remote sensing

MDPI

Article

A Novel Chaotic-NLFM Signal under Low Oversampling Factors for Deception Jamming Suppression

Jianyuan Li [1,2], Pei Wang [1,*], Hongxi Zhang [3], Chao Luo [1], Zhenning Li [1] and Yihai Wei [1,2]

[1] Department of Space Microwave Remote Sensing System, Institute of Aerospace Information Research, Chinese Academy of Sciences, Beijing 100094, China; lijianyuan21@mails.ucas.ac.cn (J.L.); luochao@aircas.ac.cn (C.L.); lizn@aircas.ac.cn (Z.L.); weiyihai22@mails.ucas.ac.cn (Y.W.)
[2] School of Electronic, Electrical and Communication Engineering, University of Chinese Academy of Sciences, Beijing 100049, China
[3] Southwest China Research Institute of Electronic Equipment, Chengdu 610036, China; zhx18800108433@163.com
* Correspondence: wangpei@aircas.ac.cn

Abstract: Synthetic aperture radar (SAR) is a high-resolution imaging radar. With the deteriorating electromagnetic environment, SAR systems are susceptible to various forms of electromagnetic interference, including deception jamming. This jamming notably impacts SAR signal processing and subsequently worsens the quality of acquired images. Chaotic frequency modulation (CFM) signals could effectively counteract deception jamming. Nevertheless, due to the inadequate band-limited performance of CFM signals, higher oversampling factors are needed for achieving optimal low sidelobe levels, leading to increased system costs and excessively high data rates. Additionally, not all chaotic sentences meet the CFM signal requirements. In response, this paper proposes a novel signal modulation method called chaotic-nonlinear frequency modulation (C-NLFM) that enhances band-limited performance. The optimum parameters for C-NLFM signals are selected using the particle swarm optimization (PSO) algorithm. In this way, C-NLFM signals attain ideal low sidelobe levels even when faced with reduced oversampling factors. Meanwhile, this chaotic coding mode retains its capability to effectively suppress deception jamming. Moreover, C-NLFM signals demonstrate versatility in adapting to various chaotic sequences, thereby enhancing their flexibility to modify the signals as required. Through comprehensive simulations, data analysis, and a semi-physical experiment, the effectiveness and superiority of this proposed method have been confirmed.

Keywords: anti-jamming; chaos; synthetic aperture radar (SAR); low oversampling factor; sidelobe suppression

check for updates

Citation: Li, J.; Wang, P.; Zhang, H.; Luo, C.; Li, Z.; Wei, Y. A Novel Chaotic-NLFM Signal under Low Oversampling Factors for Deception Jamming Suppression. *Remote Sens.* **2024**, *16*, 35. https://doi.org/10.3390/rs16010035

Academic Editor: Stefano Tebaldini

Received: 22 September 2023
Revised: 5 December 2023
Accepted: 14 December 2023
Published: 21 December 2023

1. Introduction

SAR stands as a cornerstone of active microwave remote sensing technology, enabling the achievement of high-resolution imaging in both the range and azimuth directions. This is made possible through pulse compression and the utilization of synthetic aperture techniques, respectively. SAR offers various benefits, including operational capabilities throughout the day and night and in all weather conditions, among others. As a result, SAR has established its significance across a spectrum of applications, finding a prominent role in the earth observation and environmental monitoring domains [1,2]. Its pertinence extends even further, encompassing its utilization in military operations. However, the effectiveness of SAR systems can be perturbed using active deception jamming, a prevalent form of interference. This technique involves manipulating intercepted SAR signals using methods like time delays and phase shifts to generate false targets [3,4]. Notably, active deception jamming demands a high degree of accuracy in capturing both the intra- and inter-pulse characteristics of the intercepted SAR signals, as well as the attributes of the targeted aircraft. Additionally, in terms of reception timing, the jamming signal naturally lags behind the SAR signal by multiple pulse intervals [3]. The high sidelobes in SAR can overshadow faint targets, while deceptive targets created by jamming signals severely disrupt scene target detection, posing a core problem for SAR image quality. Therefore, it is imperative to enhance the anti-jamming capability of SAR signals and minimize the possibility of interception, while maintaining the pulse compression characteristics of low sidelobes. This represents a pivotal challenge within the domain of SAR signal design technology.

Instead of using linear frequency modulation (LFM) signals, employing radar signals with a more intricate structure, heightened unpredictability, increased diversity, constrained energy, and enhanced orthogonality can enhance anti-jamming efficacy [5–7].

Although the LFM signal is the most commonly used signal in SAR, it cannot suppress deception jamming signals. For deception jamming suppression, M. Soumekh from the State University of New York created the LFM signal with mild phase perturbation to form a quadrature signal set [5]. On this foundational idea, a composite modulated signal that combines LFM signal with phase coding (LFM-PC) was proposed; nevertheless, both the LFM-phase perturbation signal and the LFM-PC signal have limited suppression impact, and further modification is required [8–11].

To address the issues raised above, many academics are interested in the study of chaotic coded signals [12,13]. A chaotic sequence is a type of random sequence produced with a nonlinear iterative mapping that is sensitive to the initial values [14]. Early on, Walker from the University of Arizona confirmed that chaotic sequences have significant auto-correlation and came to the conclusion that chaotic coded signals are appropriate for radar systems [15]. Chaotic coded signals have considerable promise for SAR signal design because they precisely match the need to create orthogonal random signals to counteract active deceptive jamming signals. In an effort to achieve a peak-to-sidelobe ratio (PSLR) of less than −40 dB for pulse compression, CFM signals applied to SAR systems have been presented [16]. The signals have great performance in reducing deception jamming signals. The SAR chaotic phase modulation (CPM) signals were also demonstrated to have the same result during the same time period [17]. Reference [18] combines chaotic sequences and LFM-PC signals, suggesting LFM phase coding with orthogonality, which yields good performance and allows interference signal suppression to be reduced to −25 dB.

Although the CFM signal has good performance in terms of low sidelobe levels and anti-interference, the random nature of its spectrum means that its spectrum envelope is no longer smooth. It has a large spectrum-hopping amplitude and the spectrum range cannot be concentrated in a specific transmission bandwidth interval. As a result, there are still certain challenges in its actual application. As in reference [17], the range oversampling rate in the simulation experiments reached 2.73 times. Reference [19] presents a method for spectrum structuring of chaotic signals based on filtering and chaos synchronization theory. A continuous CFM signal is used as the foundation in reference [20], beginning with the design of the signal spectrum, changing the time scale transformation function, modulating the frequency of the circuit, and achieving the goal of outputting a CFM signal with an arbitrary spectrum structure.

In spite of the spectrum performance being regulated in the preceding studies, it is imperative to recognize that this regulation substantially alters the structure of the emission signals, which leads to the occurrence of a slight mismatch filtering of the signal.

Therefore, following a comprehensive analysis of the current research on CFM and NLFM signals, C-NLFM signals are presented from the standpoint of designing emission signals, which can address the need to balance low sidelobe levels, anti-interference, limited spectrum bandwidth, and flexibility. C-NLFM signals are based on NLFM signals, introducing chaotic sequences to modulate the frequency, with the modulation parameters optimized using a PSO algorithm. The introduction of hyperchaotic sequences significantly enhances the randomness and unpredictability of the signal. By adjusting the initial value of the chaotic sequence, a set of signals simulating SAR emission signals is generated. The experimental results demonstrate that C-NLFM signals, using various chaotic sentences, efficiently suppress unmatched jamming signals after pulse compression and superposition, even at low oversampling factors, all while maintaining low sidelobe levels.

For clarity, the contributions in this work are summarized as follows:

- A model for chaotic encoding of time-frequency functions is introduced with a limited number of adjustable parameters. Multi-objective functions are created utilizing the average auto-correlation of a set of C-NLFM signals and the summation of their cross-correlation values. The functions are subsequently employed in the PSO algorithm for the selection of optimal parameters.
- With the use of the C-NLFM signals for SAR point target imaging under low oversampling factors, the PSLR of the range profile can be reduced to −45 dB. This reduction results from the ability of C-NLFM signals to suppress random sidelobes, leading to an overall improvement in the quality of SAR imaging.
- Our method exhibits efficient performance in suppressing deception jamming to −29 dB, with sensitivity to the initial value of the chaotic sequence. Various types of chaotic mappings can be utilized for signal encoding to enhance complexity, including the hyperchaotic mapping introduced in this paper.

The remainder of the paper is structured as follows. In Section 2, a brief overview of the technique for demonstrating a CFM signal is presented. In Section 3, the design method for the C-NLFM signal is presented along with the construction of a cubic–sine two-dimensional hyperchaotic mapping. Additionally, the way to suppress the active deception jamming signal for the proposed SAR signal is provided. In Section 4, the simulation results are given to demonstrate the applicability and interference suppression efficiency of the C-NLFM signal, and a semi-physical experiment proves the feasibility further. In Section 5, the conclusions are presented.

2. Overview of CFM Signals

CFM signals, as the name implies, use chaotic sequence values as their instantaneous frequencies, with a naturally occurring auto-correlation [21,22]. Chaotic sequences vary, and not all of them may be suitable for CFM signals, as suitability is related to the distribution of a sequence's samples. Furthermore, most CFM signals do not have well-defined limits within their spectrum bands, potentially leading to disappointing performance.

N samples of a one-dimensional chaotic sequence, denoted $x_1, \ldots, x_n, \ldots, x_N$, can be regarded as the iterative outcomes of a certain algorithm, which can be defined as

$$x_{n+1} = f(x_n), \tag{1}$$

where x_n takes on a range of values and f represents the operation of a chaotic mapping. The instantaneous frequencies of CFM signals can be expressed as

$$f_{CFM}(n\Delta t) = B_r \cdot (x_n - \alpha)\beta, \tag{2}$$

where Δt represents the time sample interval and B_r represents the signal bandwidth. Additionally, α and β are parameters that ensure the value of $(x_n - \alpha)\beta$ can be in the range of $[-0.5, 0.5]$. As a result, the discrete form of the CFM signal can be given as

$$S_{CFM}(n\Delta t) = A \cdot e^{j2\pi B_r \sum_{i=1}^{N} [(x_n - \alpha)\beta \cdot \Delta t + j2\pi f_0 \cdot \Delta t]}, \tag{3}$$

where A represents the signal amplitude while f_0 signifies the signal carrier frequency. A flowchart illustrating the entire process for generating CFM signals is presented in Figure 1. This process involves chaotic encoding to create digital frequency modulation signals, subsequently converting them into analog signals.

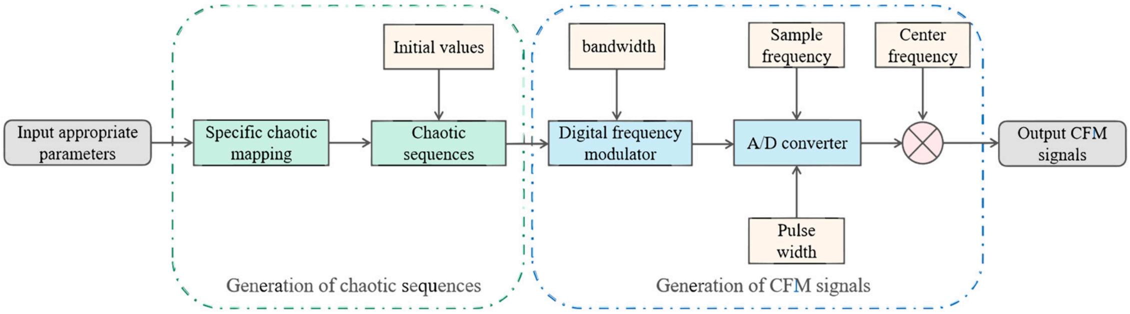

Figure 1. Flowchart of producing CFM signals.

Several techniques exist for spectrum analysis of signals, including direct spectrum estimation using discrete Fourier transform, spectrum estimation through AR models, the music algorithm, and others. In cases where the sample frequency falls below the Nyquist sample frequency, higher-frequency signal components shift to lower frequencies. Considering that most CFM signals have high-amplitude, high-frequency components that extend beyond the bandwidth, insufficient oversampling can result in spectrum aliasing and spreading.

3. Model of the C-NLFM Signal

Given the aforementioned issues, this chapter proposes a coding method that involves the amalgamation of NLFM signals and chaotic sequences. The objective is to standardize the band-limited performance of the spectrum, while simultaneously preserving the essential characteristics of chaotic coding signals. To begin with, this chapter presents the coding method in detail for designing a C-NLFM signal. Subsequently, the discussion focuses on the selection of an appropriate chaotic sequence for implementation. Lastly, this chapter concludes with an exploration of signal spectrum analysis.

3.1. Introduction to C-NLFM Signal Design

The prevalent NLFM signal within SAR systems is commonly crafted through the manipulation of the amplitude spectrum subsequent to the signal's pulse compression output. This design consideration prevents mismatches in matched filtering and suppresses sidelobes, in contrast to the LFM signal when a window function is introduced [23]. This signal demonstrates a nonlinear relationship between frequency and time, featuring rapid shifts at the extremities of the pulse duration range and gradual transitions within the middle. It possesses a configuration reminiscent of an inverse "S" shape. To initiate the process, the selection of a window function determines the amplitude spectrum of a nonlinear time-frequency function. For instance, the Hamming window function $W(f)$ can be represented as

$$W(f) = 0.54 + 0.46cos(2\pi f/B_N), \tag{4}$$

where B_N is the bandwidth specified in the design of the NLFM. The relationship connecting the group time delay function $T(f)$ and the squared amplitude spectrum $U^2(x)$ can be derived using the standing phase principle as

$$T(f) = K\int_{-\infty}^{f} U^2(x)dx. \tag{5}$$

where K is a constant. By letting $\mathrm{U}^2(\mathrm{f})$ be equal to $\mathrm{W}(\mathrm{f})$, the group time delay function $\mathrm{T}(\mathrm{f})$ at the pulse length T_0 can be determined as

$$T(f) = \frac{T_0}{B_N}f + \left(\frac{0.426T_0}{\pi}\right)sin\left(\frac{2\pi f}{B_N}\right). \tag{6}$$

The time-frequency function $f_N(t)$ of the signal and the group time delay function $T(f)$ form an approximate pair of inverse functional relationships. In other words, the time-frequency function of the signal can be expressed as

$$f_N(t) = T^{-1}(f). \tag{7}$$

Furthermore, the time-frequency function can be approximated using segmented linear interpolation to determine the polynomial coefficients $b_0,\ b_1,\ b_2, \cdots, b_U$ of $f_N(t)$, expressed as

$$f_N(t) = b_0 + b_1 x + b_2 x^2 + \ldots + b_U x^U, \tag{8}$$

where $1,\ \ldots,\ U$ are polynomial orders.

When creating the C-NLFM signal, a chaotic sequence of amplitude modulation is employed to encode the instantaneous frequency of NLFM at each individual sample point. This approach results in a signal characterized by chaotic random jitter in its time-frequency function, ultimately forming an inverse "S" shape. At this stage, the signal can be conceptualized as a composite of multiple short-time LFM signals. Each of these LFM signals possesses a chirp rate that varies in accordance with the specified coding way.

Utilizing the $x(n)$ sequence from a specific chaotic mapping, the amplitude modulation of the chaotic sequence $x(n)$ is governed by two parameters, namely, A and B, which influence the magnitude of the jitter. Various optimization algorithms can be employed to select the parameters A and B in order to minimize PSLR and jamming suppression. Examples of such algorithms include PSO, genetic algorithms (GAs), and more. The modulation process of $X(n)$ can be mathematically expressed as

$$X(n) = (x(n) + A) \cdot B, \tag{9}$$

where $n = 1,\ 2,\ \ldots,\ N$. For different initial values, distinct sequences of $X(n)$ can be obtained as $X_1(n),\ X_2(n),\ \ldots,\ X_M(n)$.

Traditional optimization approaches face limitations stemming from problem-specific characteristics, sensitivity to initial values, and potential inefficacy in high-dimensional or intricate problem settings. With the advancement of the field of machine learning and deep learning, heuristic optimization methods, including genetic algorithms, simulated annealing, and particle swarm optimization (PSO), have gained prominence as essential optimization techniques. PSO, in particular, is characterized by its rapid search speed, high efficiency, and straightforward algorithm.

In order to determine the parameters A and B, using the PSO algorithm as a choice, the selection of influencing factors serves as the objective functions. These objective functions include the average PSLR of the auto-correlation functions for each signal and the summation of cross-correlations among a set of emission signals denoted as $S_1,\ S_2,\ \ldots,\ S_M$, modulated by $X_1(n),\ X_2(n), \ldots,\ X_M(n)$, respectively. The objective function model is formulated as

$$PSLR\_S_m = 10log_{10}\frac{I_b}{I_a}, \tag{10}$$

$$min\left[\frac{\sum_{m=1}^{M} PSLR\_S_m}{M}\right], \tag{11}$$

$$min\max_{\tau}\left[\sum_{m1 \neq m2} C_{m1,m2}(\tau)\right], \tag{12}$$

where $m = 1,\ 2,\ \ldots, M$ and I_a as well as I_b represent the amplitude of the main lobe and the first sidelobe of the auto-correlation function of S_m, respectively. $C_{m1,m2}(\tau)$ denotes the cross-correlation function value between signals S_{m1} and S_{m2} at time τ.

By multiplying the previously derived inverse "S"-shaped nonlinear time-frequency function with the amplitude-modulated chaotic sequence, the resulting signal obtains a new frequency coding, defined as

$$\omega_r(n) = X(n)\cdot f_N(n), \tag{13}$$

where $f_N(n)$ represents the discrete version of the instantaneous frequency of the NLFM signal derived from Equation (8). At this juncture, the intra-pulse signal bandwidth can be expressed as

$$B_r = B_N\cdot\{max[X(n)]\}, \tag{14}$$

Therefore, the discrete representation of the intra-pulse FM pulse within a pulse period can be formulated as

$$S(n\Delta t_r) = \sigma\cdot e^{j2\pi\Delta t_r\{nf_0+\sum_{i=1}^{n}\omega_r(n)\}}, \tag{15}$$

where $n\Delta t_r$ stands for the intra-pulse time length, f_0 represents the constant carrier frequency, and σ signifies the pulse amplitude. Figure 2 displays the time-frequency function and phase function plots of the simulated C-NLFM signal. As observed, Figure 2a portrays random jitters in the inverse "S"-shaped time-frequency function curve, with the contribution of the chaotic sequence. Meanwhile, Figure 2b presents phase jitter, introducing randomness and anti-jamming characteristics to the signal. Furthermore, the jitters also complicate the recognition of the signal parameters by jammers.

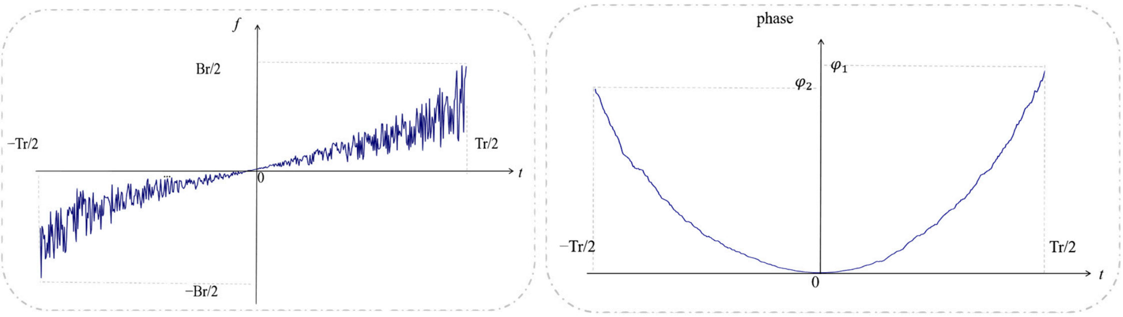

(**a**) (**b**)

Figure 2. Intra-pulse time-domain characteristics of the C-NLFM signal. (**a**) Instantaneous frequency change of C-NLFM signal; (**b**) iinstantaneous phase change of C-NLFM signal.

3.2. Introduction of Two-Dimensional Hyperchaotic Sequence

In the field of radar signals, when it comes to CFM signals, one-dimensional chaotic mappings that can be employed include Bernoulli chaotic mapping, logistic chaotic mapping, tent chaotic mapping, cubic chaotic mapping, sine chaotic mapping, and others [24–27]. These mappings are detailed in Table 1. The sequences generated by these chaotic mappings exhibit favorable auto-correlation properties and are straightforward to implement. However, the inherent simplicity of their repetitive calculations imposes constraints on the attainable complexity of the signals [28].

Table 1. One-dimensional chaotic mapping.

Mapping Name	Mapping Relation
Bernoulli	$x_{n+1} = \begin{cases} 2x_n + 0.5 & -0.5 < x_n < 0 \\ 2x_n - 0.5 & 0 \le x_n < 0.5 \end{cases}$
Logistic	$x_{n+1} = 4x_n(1 - x_n)$
Tent	$x_{n+1} = \begin{cases} 0.5 + 2x_n & -0.5 < x_n < 0 \\ 0.5 - 2x_n & 0 \le x_n < 0.5 \end{cases}$
Cubic	$x_{n+1} = 3x_n(1 - {x_n}^2)$
Sine	$x_{n+1} = sin(\pi x_n)$

The straightforward operations of cubic chaotic mapping and sine chaotic mapping allow for their amalgamation into a novel two-dimensional hyperchaotic mapping [29,30]. This integration augments computational complexity, thus enhancing the unpredictability of the sequences. This leads to an interrelationship between the two dimensions in which they both influence each other. The mapping equation for the cubic–sine two-dimensional hyperchaotic mapping can be expressed as

$$\begin{cases} x(n+1) = sin[r \cdot \pi x(n)] \cdot \left\{ 1 - \frac{sin[\pi y(n)]^2}{2} \right\} \\ y(n+1) = sin[r \cdot \pi y(n)] \cdot \left\{ 1 - \frac{sin[\pi x(n+1)]^2}{2} \right\} \end{cases}, \tag{16}$$

where r represents the mapping parameter, with x and y constrained to the interval $[-1, 1]$.

The Lyapunov exponent is an important measure of the complexity of chaotic mappings. A mapping earns the label "hyperchaotic" when it encompasses an n-dimensional nonlinear structure with n-Lyapunov exponents, with the stipulation that the count of positive Lyapunov exponents surpasses two [31]. Figure 3 illustrates the two Lyapunov exponents of the cubic–sine two-dimensional hyperchaotic mapping obtained through analysis with the Jacobian matrix. For a specific value of the parameter r, both Lyapunov exponents λ_1 and λ_2 display positive values, indicating the mapping's hyperchaotic state. Taking initial values of x and y as 0.1, 0.3, 0.5, and 0.7 across four instances, the x-sequence and y-sequence values are tracked after 2000 calculation iterations.

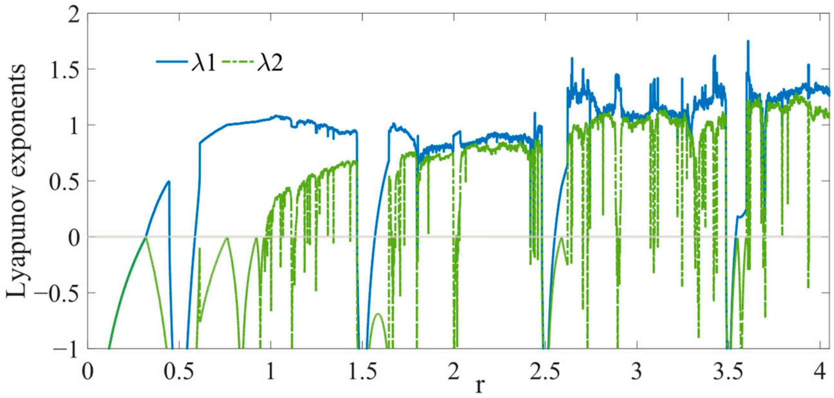

Figure 3. Lyapunov exponents of the cubic–sine two-dimensional hyperchaotic mapping.

The cubic–sine two-dimensional hyperchaotic sequences have a defined range of values, and the pairs are uniformly distributed within a given range, drawing attention to the variability of the data, as evident in Figure 4. When the initial values are modified, the distribution of the x-sequence and y-sequence values also changes, thereby demonstrating the initial-value sensitivity of the chaotic sequence.

When compared to conventional chaotic mappings, hyperchaotic mappings demonstrate more evident chaotic and random properties, making them particularly valuable for applications such as countering enemy reconnaissance [17].

It is important to highlight that, while the cubic–sine two-dimensional hyperchaotic mapping might not perform optimally when applied to CFM signals, its performance remains unaffected in the context of C-NLFM. This distinction arises from the fact that C-NLFM necessitates only an encrypted jitter. In C-NLFM signals, the jitter is both well-defined and indispensable. Treating it as an approximate NLFM for the purpose of matched filtering would yield mismatched outcomes and inaccurate imaging. Consequently, the intricate nature of the jitter underpins the limited interceptibility and inherent unpredictability of C-NLFM signals. This facet thereby opens the door for the application of numerous intricate sequences derived from complex chaotic mappings.

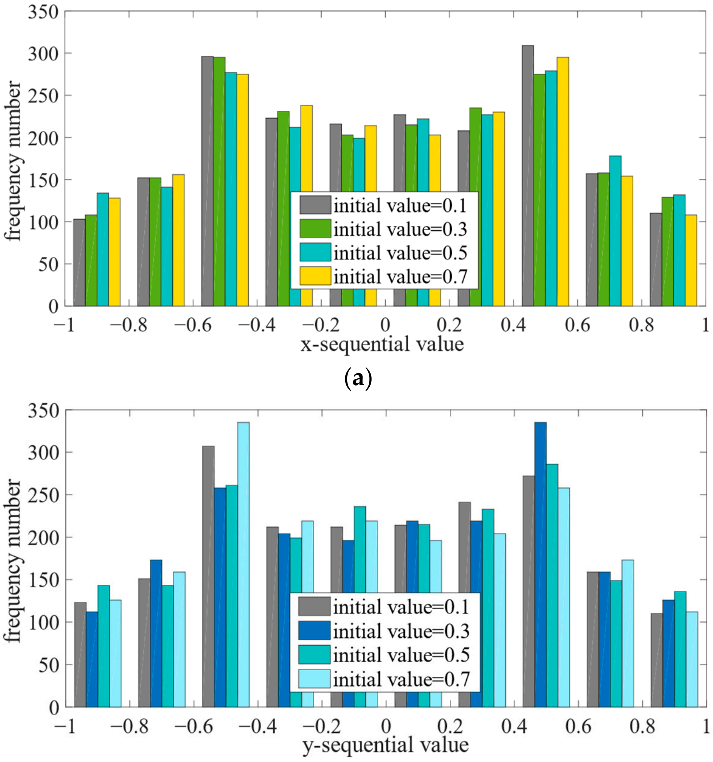

(**a**)

(**b**)

Figure 4. Cubic–sine two-dimensional hyperchaotic mapping outputs with different initial values. (**a**) x-sequence output; (**b**) y-sequence output.

3.3. Analysis of Signal Spectrum

Due to the regularity in the frequency trend of the C-NLFM signal, its spectrum demonstrates less randomness when compared to the CFM signal. Consequently, the C-NLFM signal demonstrates a spectrum performance that is bandlimited, resembling the characteristics of the NLFM signal. This section presents the spectrum analysis of four distinct signals: LFM, NLFM [23], Bernoulli-FM [16,32], tent-FM [33], and C-NLFM, as depicted in Figure 5. During the simulation, the parameters A and B for the C-NLFM signal are set to 8 and 9000, respectively. The bandwidth is set to 5 GHz, the pulse width to 30 μs, and the oversampling factor to twice the bandwidth.

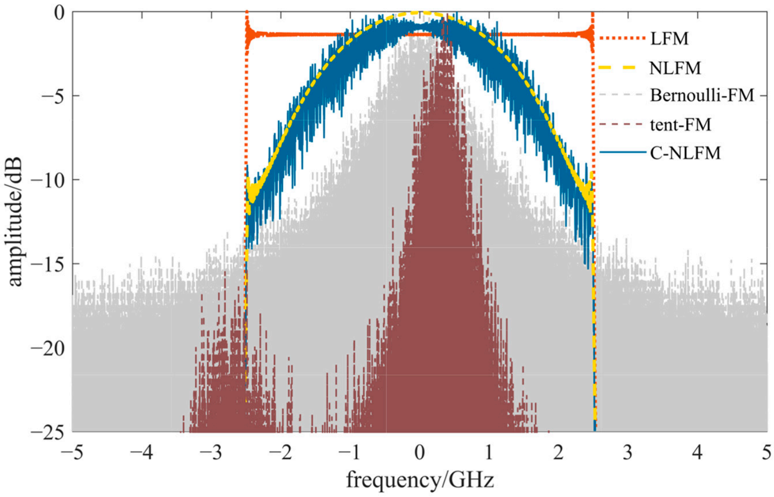

Figure 5. Normalized spectrum of LFM signal, NLFM signal [23], Bernoulli-FM signal [16,32], tent-FM signal [33], and C-NLFM signal.

The spectrum of the CFM signal lacks a clear bandwidth boundary, and the compressed pulse waveforms are prone to the side flaps fusing into the main flap at low oversampling factors. Fortunately, this deficiency is compensated for by the C-NLFM signal. Its spectrum envelope resembles that of NLFM, with the inclusion of random jitter originating from its chaotic modulated frequency component.

In this way, the C-NLFM signal is strategically developed for practical applications while simultaneously delivering superior imaging quality and a highly effective anti-jamming capability.

3.4. Method of Low Sidelobe and Anti-Jamming

Several SAR imaging algorithms exist, such as the RDA, CSA, wKA, and BPA algorithms. RDA represents the most conventional imaging algorithm. Both CSA and wKA are improved frequency domain algorithms that achieve higher accuracy [34,35]. Ref. [35] extended the widely used wKA based on LBF, yielding high-resolution results akin to those achieved by BPA.

Among these, the BPA algorithm provides the most intuitive insight into the process of superimposing different azimuthal pulses during imaging. In the BPA algorithm, the echo signals from numerous pulses are collected. After undergoing pulse compression and Doppler frequency compensation, these pulses are synchronized in the time domain. Subsequently, each pulse is projected in the azimuthal direction, and its energy is allocated to the corresponding pixel. These energy-assigned pulses are then superimposed at the pixel's location, resulting in the accumulation of energy from multiple pulses. This accumulation enhances the energy of the target echo signal.

Based on the imaging principle, PSLR and the integrated sidelobe ratio (ISLR) between a single pulse and multiple pulses can only be maintained if the main lobe and sidelobes of the pulses remain constant, precisely like the LFM signal.

The sensitivity of a chaotic sequence to its initial value entails that altering the starting value leads to modifications across the entire sequence. However, this adjustment does not impact the interval range or probability density distribution of sequence values. Consequently, it leaves the sequence's auto-correlation and cross-correlation features unaffected. Similarly, the sensitivity to the starting value is retained for the C-NLFM signal, allowing the jitter distribution to be altered when the initial value is changed.

By carefully adjusting the initial value in the azimuthal direction and transmitting distinct C-NLFM signals $(S1,\ S2,\ldots)$, a collection of signals is generated. These signals share the same primary characteristics but exhibit varying jitter distributions.

Figure 6 illustrates a schematic representation of the auto-correlation of signals $S1,\ S2,\ldots$, as well as their cross-correlation. The blue part represents the low amplitude energy and the green part represents the high amplitude energy. In Figure 6a, the auto-correlation performance is showcased. Upon adjusting the initial value, the set of signals undergoing pulse compression exhibits nearly identical main lobes, while the sidelobes exhibit random jitter. As multiple pulses are superimposed, the main lobe's amplitude increases significantly, while the sidelobes disperse the energy from each other. This enhances the amplitude ratio of the main lobe to the sidelobes, resulting in the appearance of a low sidelobe level.

Figure 6b illustrates the cross-correlation performance, representing the disparity between the deceptive jamming signal and the real signal. Notably, the waveforms, when cross-correlated with each other, also display randomness. Upon superimposition, these signals can mutually disperse the energy from each other, leading to a final amplitude considerably lower than that achieved through real signal pulse compression and main lobe superimposition. This suppression effect serves to counteract the influence of deceptive jamming signals.

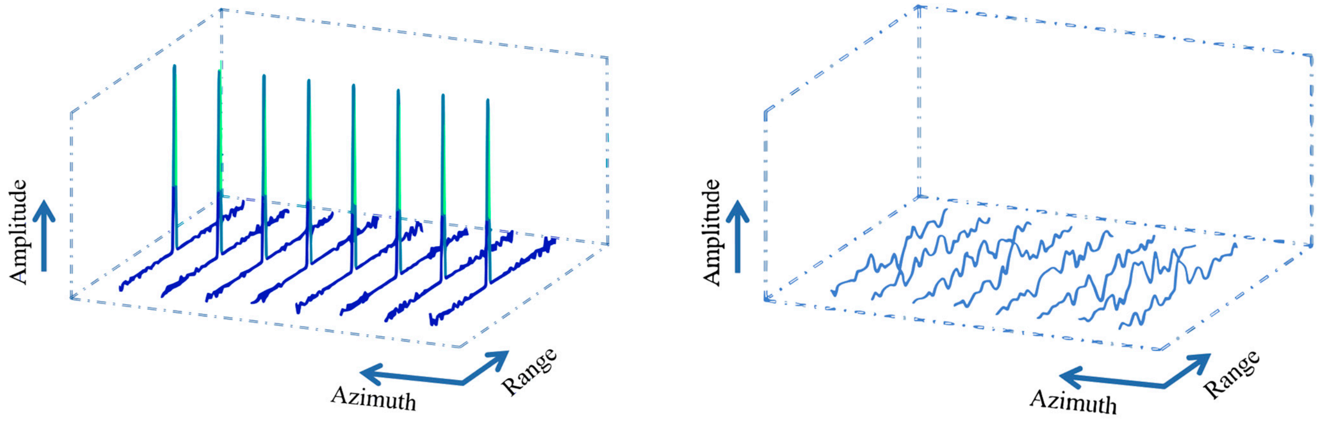

(**a**) (**b**)

Figure 6. Diagrams illustrating the auto-correlation and cross-correlation of C-NLFM signals with distinct initial values. (**a**) Auto-correlation diagram; (**b**) cross-correlation diagram.

4. Simulation and Analysis

In this chapter, the effectiveness of the C-NLFM signal in achieving a low sidelobe level and anti-interference capabilities is separately validated. To verify the low sidelobe characteristics of the C-NLFM signal, a comparison is conducted with several widely used signals. Additionally, the validation of the C-NLFM signal's resistance to deception jamming signals involves a comparison with existing studies that focus on signal coding to counter deception jamming signals. Finally, the results of the semi-physical experiment are presented.

4.1. On the Pulse Compression Performance of the Waveform

The pulse compression performance of the signals is examined by incrementally varying the oversampling factor within the range of 1.1 to 3, with a bandwidth of 500 MHz and a pulse width of 20 µs. Multiple CFM signals are selected to be compared with C-NLFM signals.

After compressing signals at different oversampling factors, variations in the PSLR and ISLR of individual pulses within the five signals become evident, as depicted in Figure 7. In this process, pulse compression of a single C-NLFM signal is performed, resulting in high random energy in the sidelobes. Therefore, in this case, some fluctuation in the value of the highest sidelobe within a certain range is acceptable.

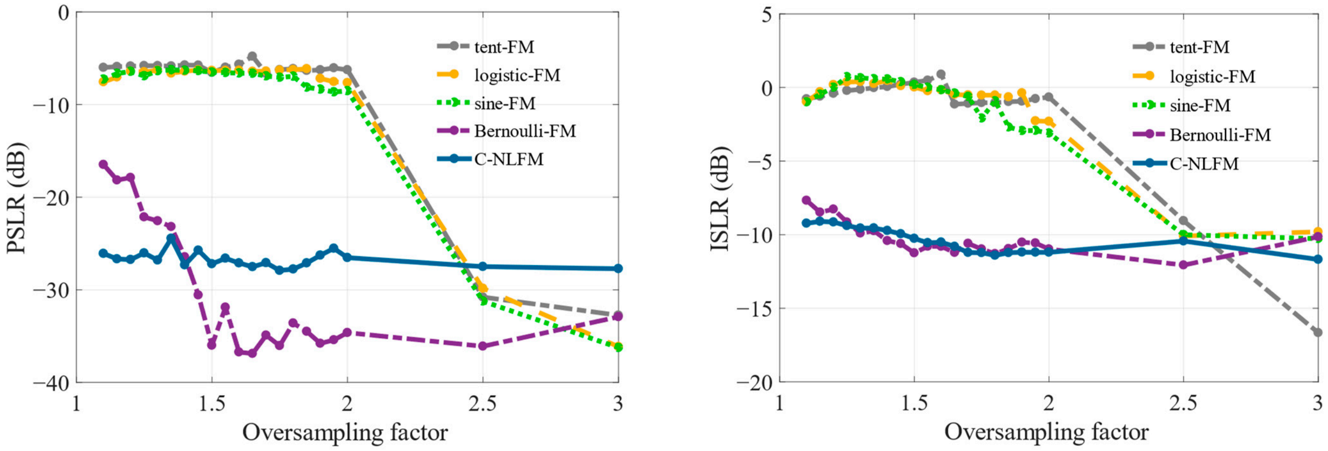

(**a**) (**b**)

Figure 7. Performance analysis of individual pulses of various types under different oversampling factors. (**a**) PSLR; (**b**) ISLR.

Particularly, at low oversampling factors, the CFM signal demonstrates prominently higher sidelobes. The optimal low sidelobe effect is attained when the oversampling factor exceeds two times. Despite the relatively superior performance of the Bernoulli-FM signal compared to other CFM signals, it also struggles to mitigate high sidelobes at low oversampling factors. In comparison, the PSLR and ISLR values of the C-NLFM signal consistently exhibit a stable state, with both values remaining notably low.

Significantly, a C-NLFM signal's sidelobes exhibit random jitter, indicating the potential to mitigate it by combining multiple signals with varied initial values of the chaotic sequence. This approach can effectively reduce the sidelobes and achieve a performance similar to that of the NLFM signal. To put it another way, the C-NLFM anti-jamming signal only necessitates a lower oversampling factor to attain decreased sidelobes following subsequent imaging steps. This not only reduces the system costs but also enhances the practicality of the signal.

Except for the signals in Figure 7, Figure 8 displays additional C-NLFM signals encoded by tent sequences and logistic sequences, as well as NLFM signals. Moreover, the signals with chaotic sequence coding exhibit variations in the azimuthal direction based on different initial values. Figure 8 demonstrates their sidelobe performance in the range profile after point imaging under different oversampling factors.

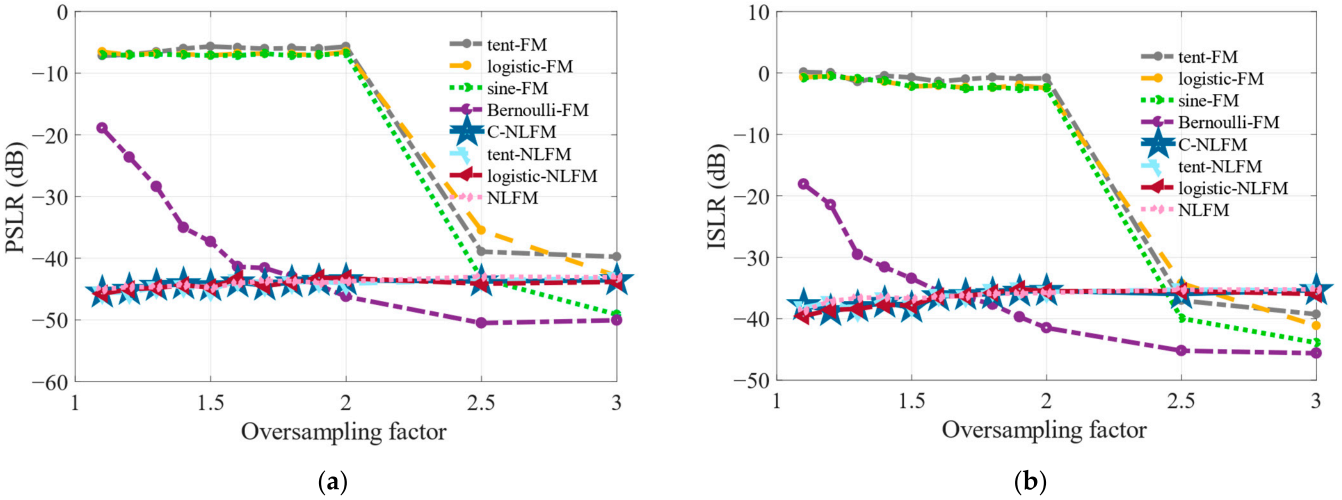

Figure 8. Performance analysis of different sets of transmitted signals in the range profile after point imaging under different oversampling factors. (**a**) PSLR; (**b**) ISLR.

Due to randomness in the sidelobes of these signals, sidelobes aligned in the time domain disperse energy during imaging. Taking Bernoulli-FM and C-NLFM as examples, both the PSLR and ISLR in Figure 8 exhibit a noticeable decrease compared to those in Figure 7 when the oversampling factor is below 1.5. However, Bernoulli-FM exhibits higher sidelobes than C-NLFM, attributed to severe spectral aliasing at lower sampling factors.

According to the experimental results, the applications of tent and logistic sequences show suboptimal performance in CFM, whereas they perform significantly better in C-NLFM. This observation underscores that C-NLFM signals can achieve the desired effects using chaotic sequences with different distributions. Consequently, the decision to increase the complexity of chaotic sequences remains unaffected, highlighting the robustness of C-NLFM signal in accommodating diverse chaotic sentences. In other words, it confirms that the C-NLFM signal enhances the flexible application of different chaotic sentences.

The imaging of point targets using the LFM signal, NLFM signal [23], Bernoulli-FM signal [32], tent-FM signal [33], and the proposed C-NLFM signal with an oversampling factor of 1.15 was simulated based on the parameters specified in Table 2. Their range and azimuth profiles are presented in Figure 9, and the evaluation metrics are summarized in Table 3, confirming the conclusions mentioned earlier.

Table 2. Parameters of simulation.

Parameter	Value
Carrier Frequency	5.3 GHz
Sensor Velocity	150 m/s
Band Width	500 MHz
Pulse Width	20 µs
Range Oversampling Factor	1.15
Azimuth Oversampling Factor	1.2
Squint Angle	0°
Closest Range	20 km

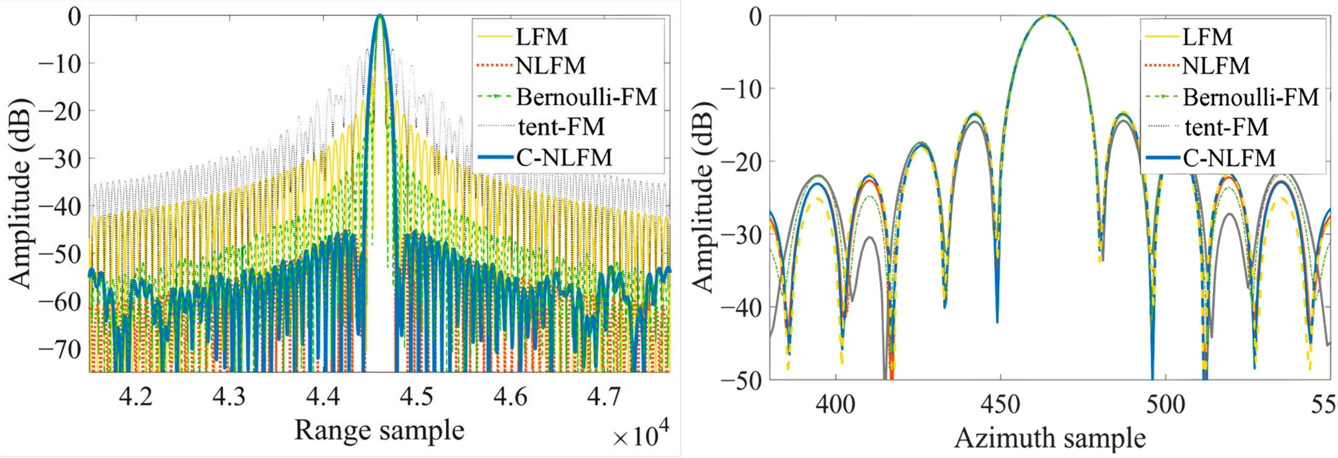

(**a**) (**b**)

Figure 9. Plots of the point target impulse response functions for various signals. (**a**) Range profile of the point target imaging result; (**b**) azimuth profile of the point target imaging result.

Table 3. Performance analysis of range and azimuth profiles with an oversampling factor of 1.15.

Signals	Range Profile			Azimuth Profile		
	PSLR (dB)	ISLR (dB)	MBF	PSLR (dB)	ISLR (dB)	MBF
LFM	−13.27	−9.71	1.0	−13.93	−9.39	1.0
NLFM [23]	−45.08	−36.91	1.5	−13.59	−10.01	1.0
Bernoulli−FM [32]	−20.62	−18.80	1.0	−13.97	−9.51	1.0
Tent−FM [33]	−7.04	−1.03	0.8	−13.99	−9.21	1.0
C−NLFM	−45.32	−32.38	1.6	−13.53	−10.02	1.0

After conducting data analysis and comparisons, it is observed that, in comparison to other signals, particularly LFM signals, the azimuth profile of the proposed signal experiences minimal changes and can be regarded as relatively unaffected, as shown in Figure 9b. The PSLR of the C-NLFM can be effectively reduced to below −45 dB, and the ISLR can be brought down to below −30 dB, as demonstrated by the range profiles illustrated in Figure 9a. Conversely, the Bernoulli-FM signal struggles to achieve similar results under these circumstances. With the addition of multiple pulses, the performance of the C-NLFM signal tends to converge toward that of the NLFM signal due to its foundational reliance on the NLFM signal. At the same time, its main lobe broadening factor (MBF) can be improved by utilizing a more effective NLFM signal. With a low oversampling factor, the point target imaging advantage of the CFM signal is no longer dominant, and the sidelobe is very easy to merge into the main lobe, which reduces the imaging quality. In contrast, C-NLFM demonstrates adaptability to a variety of complex environments.

4.2. On the Suppression Performance of the Deception Jamming

The anti-active deception jamming performance of the C-NLFM signal is validated by comparing it with the LFM signal, RNLFM signal [36], and LFM-PC signal [18]. In this simulation, the transmitted signal's range oversampling factor is set to 1.15 with a bandwidth of 1 GHz. The simulation comprises thirteen real point targets arranged in the shape of a "+" along with six false point targets positioned diagonally. Due to LFM's limited ability to counter active deception jamming signals, the false point targets marked in the red dotted box persist in Figure 10a. Additionally, the suppression results of other signals are also marked by the corresponding red dotted box.

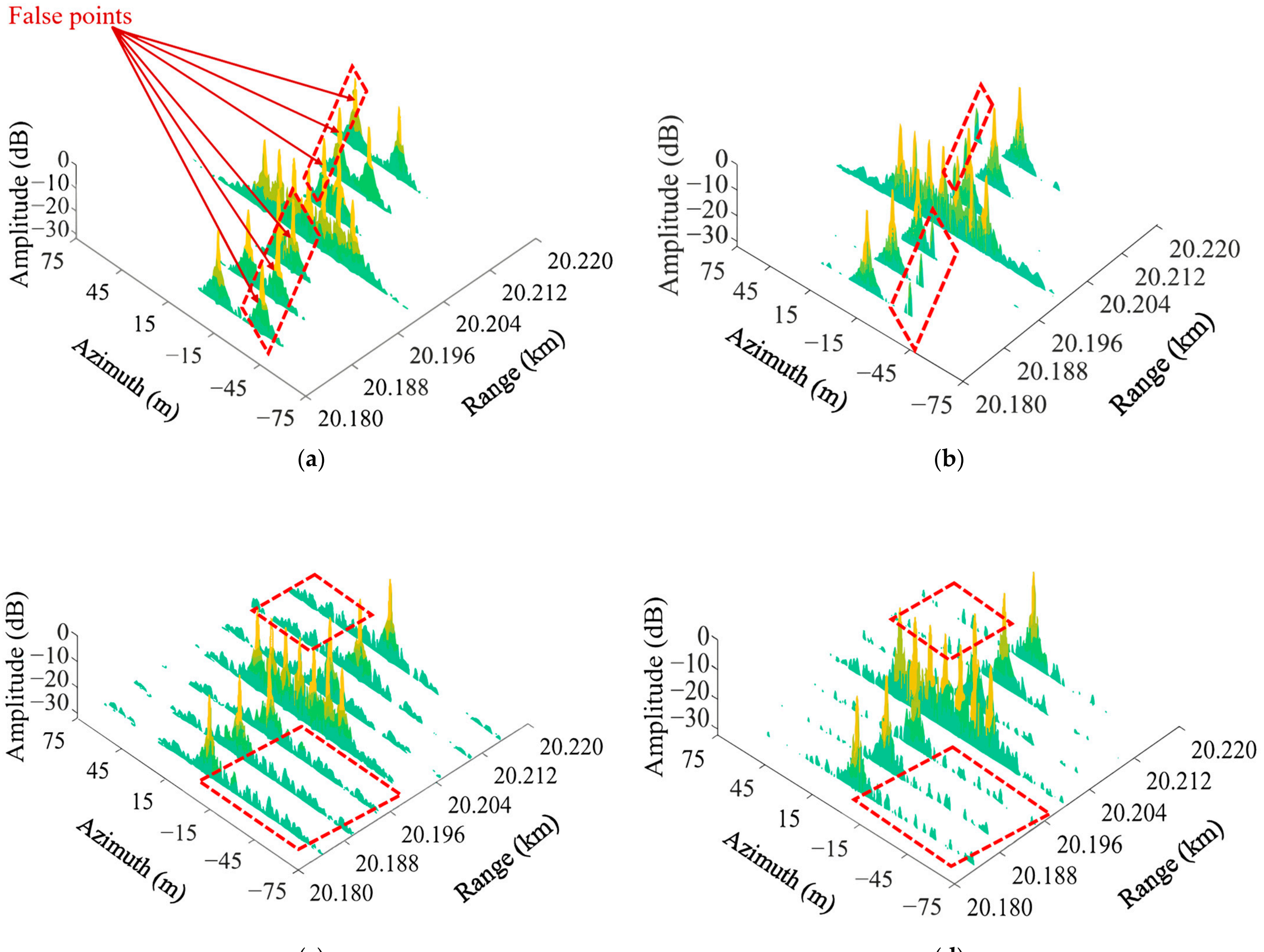

(**a**) (**b**)

(**c**) (**d**)

Figure 10. Suppression of false point targets results. (**a**) LFM; (**b**) RNLFM [36]; (**c**) LFM-PC [18]; (**d**) C-NLFM.

The jamming-to-signal ratio (JSR) can measure an amplitude gap between the suppressed jamming signals and the real signals. The results are demonstrated in Table 4, with a comparison of various signals. In contrast, LFM does not have the ability to suppress the deception jamming. As composite modulation signals, C-NLFM can bring out the obvious advantage in deception jamming suppression. In Figure 10b, the RNLFM [36] signal is generated by irregularly segmenting the signal and changing the frequency polarity, resulting in multiple waveforms. RNLFM [36] signals can reduce the amplitude of deceptive jamming signals in imaging. However, they may still be mistaken for potential targets. In contrast, both the LFM-PC [18] and C-NLFM signals lead to a complete mismatch of deceptive jamming signals, making their suppression effects more desirable, as shown in Figure 10c,d. Additionally, the C-NLFM signal further reduces the jamming signal's sidelobes by an additional 5 dB to −29 dB.

Table 4. Performance analysis of JSR.

Signals	JSR (dB)
LFM	0
RNLFM [36]	−21.08
LFM-PC [18]	−24.22
C-NLFM	−29.64

Figure 11 depicts a simulated image generated by emitting NLFM and C-NLFM signal groups, with the goal of contrasting the suppression result of a false target within a simulated SAR scanning region. The scene for the surface target simulation is an airport, and the arrows in Figure 11 indicate the direction of range and azimuth. In Figure 11a, an NLFM signal is employed, while in Figure 11b, a C-NLFM signal is utilized. In this scenario, a total of eight aircrafts are parked on both the upper and lower sides and are outlined in yellow. The aircraft in the center of Figure 11a represents a false target and are outlined in red, effectively suppressed in Figure 11b. The suppression result is indicated by red boxes. Following suppression, the deception jamming signals transform into clutter in the surrounding imaging area. Consequently, the false target model becomes entirely shapeless. The simulation results confirm the effectiveness of the C-NLFM signal groups in successfully countering active deception jamming.

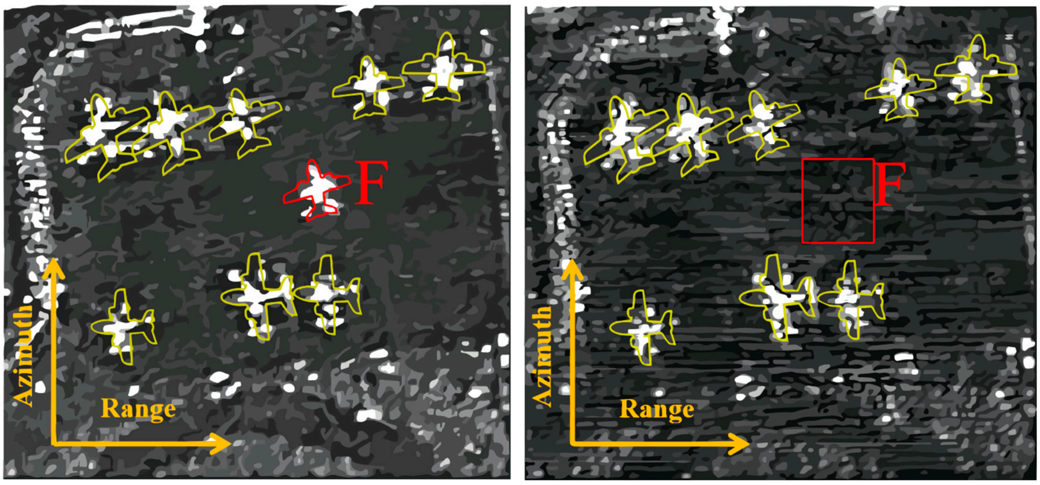

(**a**) (**b**)

Figure 11. Results of suppressing the false targets. (**a**) Imaging with NLFM signal; (**b**) imaging with C-NLFM signal.

4.3. On the Experiment of the Semi-physical Simulation System

The system is configured to produce I/Q base-band C-NLFM signals with a bandwidth of 500 MHz and an oversampling factor of 1.15. The complete procedure of the semi-physical experiment is shown in Figure 12. The primary equipment for this experiment comprises a personal computer (PC), an arbitrary waveform generator (AWG), a spectrum analyzer, and an oscilloscope, as displayed in Figure 13.

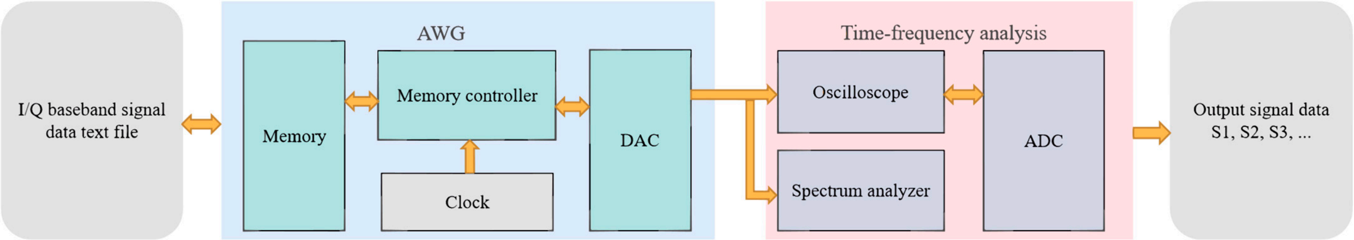

Figure 12. System of the semi-physical simulation experiment.

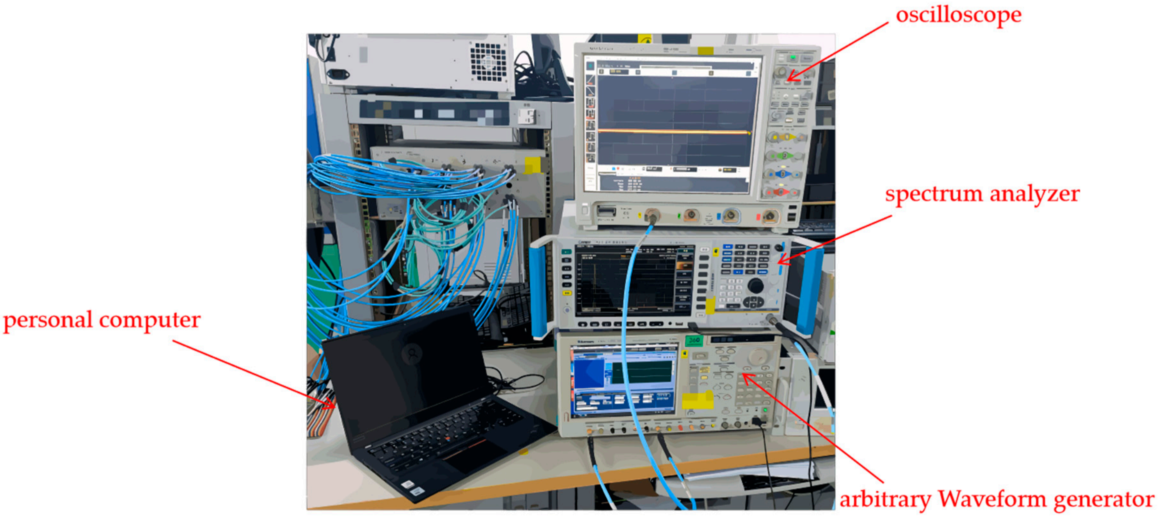

Figure 13. The primary equipment for the semi-physical experiment.

C-NLFM signal groups can be simulated by developing algorithms on a PC in advance. Subsequently, the generated data can be uploaded into the memory of the AWG. The signal data stored in memory can be retrieved at an appropriate clock frequency before being sent to a digital-to-analog converter (DAC) for analog signal output. These analog signal outputs are fed into an oscilloscope and spectrum analyzer to conduct time-frequency analysis of the signals, and the results are presented in Figure 14, closely resembling the previously simulated results. The analog signals from the oscilloscope can be sent to an analog-to-digital converter (ADC) for conversion into digital signals, which can then be saved.

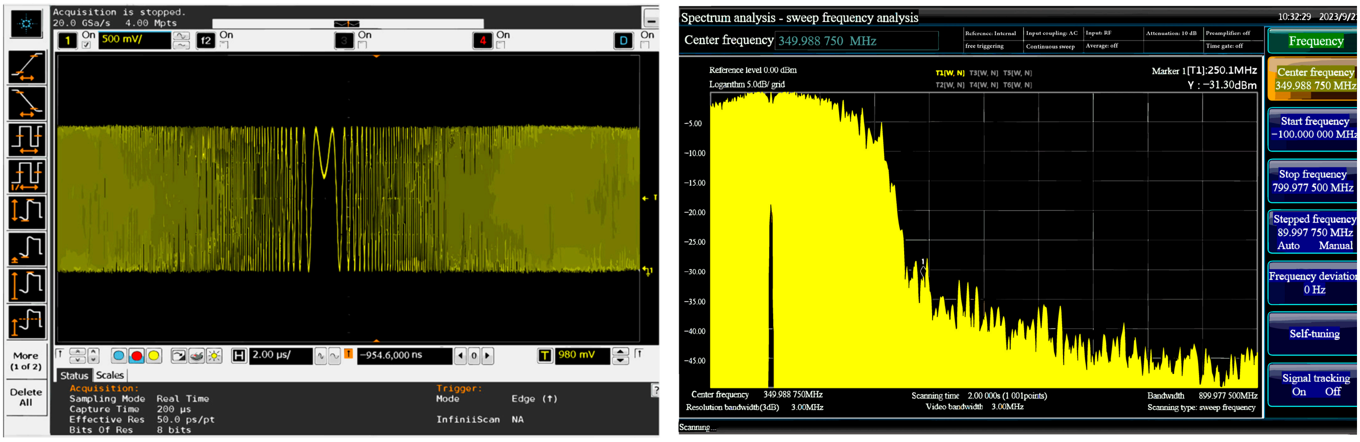
Acquisition is stopped.
20.0 GSa/s 4.00 Mpts
1 On 500 mV/
H 2.00 µs/
−954.6,000 ns
T 980 mV
Acquisition:
Sampling Mode Real Time
Capture Time 200 µs
Effective Res 50.0 ps/pt
Bits Of Res 8 bits
Trigger:
Mode Edge (↑)
InfiniiScan NA

Spectrum analysis - sweep frequency analysis
10:32:29 2023/9/2
Center frequency 349.988 750 MHz
Reference: Internal
free triggering
Input coupling: AC
Continuous sweep
Input: RF
Average: off
Attenuation: 10 dB
Preamplifier: off
Time gate: off
Reference level 0.00 dBm
Loganthm 5.0dB/ grid
Marker 1[T1]:250.1MHz
Y : −31.30dBm
Center frequency 349.988 750MHz
Resolution bandwidth(3dB) 3.00MHz
Scanning time 2.00 000s (1 001points)
Video bandwidth 3.00MHz
Bandwidth 899.977 500MHz
Scanning type: sweep frequency
Center frequency 349.988 750 MHz
Start frequency −100.000 000 MHz
Stop frequency 799.977 500 MHz
Stepped frequency 89.997 750 MHz Auto Manual
Frequency deviation 0 Hz
Signal tracking On Off
Scanning ...

(**a**) (**b**)

Figure 14. Time-frequency analysis of C-NLFM signal generated from AWG. (**a**) Time analysis of C-NLFM signal; (**b**) frequency analysis of C-NLFM signal.

A single base-band NLFM signal and fifty base-band C-NLFM signals are generated using distinct initial values of a chaotic sequence. Figure 15 compares the simulation results of real and false signals using both NLFM and C-NLFM signals. Figure 15a,b respectively depict the superimposed results of NLFM and C-NLFM signals after pulse compression. The signals obtained through the semi-physical experiment are repeatedly transmitted until they meet the requirements of a synthetic aperture. Figure 15c,d present the imaging outcomes.

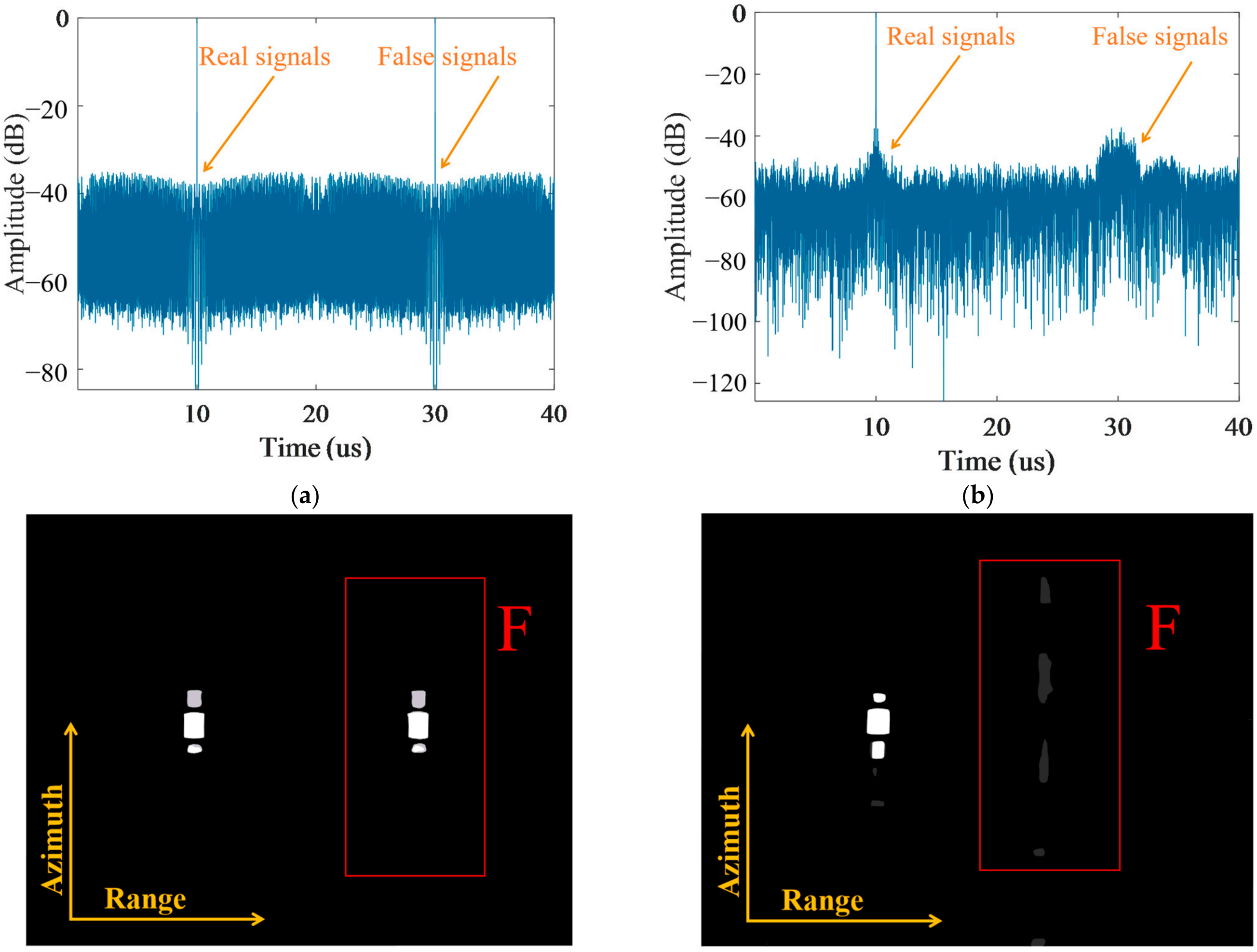

(a) (b)

(c) (d)

Figure 15. Validation of deceptive jamming suppression with semi-physical experiment. (**a**) Superimposed result of NLFM signals after pulse compression; (**b**) superimposed result of C-NLFM signals after pulse compression; (**c**) imaging result of NLFM signals; (**d**) imaging result of C-NLFM signals.

These results demonstrate that NLFM signals, as theoretically analyzed, are ineffective at suppressing false signals, while emphasizing the practical potential of C-NLFM signals in application.

5. Conclusions

This paper introduces a novel coding method designed to suppress active deception jamming while achieving favorable imaging performance, contrasting with traditional CFM signals, which exhibit high sidelobes under low oversampling factors. The proposed method utilizes hyperchaotic sequence frequency modulation of NLFM signals, enhancing the spectrum band-limited performance while preserving the randomness of chaotic coding. Consequently, it achieves reduced sidelobes even at a low oversampling factor of 1.15. Importantly, this method capitalizes on the sensitivity of chaotic initial signal values, generating a diverse collection of signals with varying phase distributions to counteract false targets. Both theoretical analysis and simulation results emphasize the effectiveness and superiority of this approach in anti-interference and imaging scenarios.

Author Contributions: Conceptualization, J.L., P.W. and H.Z.; Methodology, J.L. and P.W.; Software, J.L. and H.Z.; Validation, J.L., H.Z., C.L., Z.L. and Y.W.; Formal analysis, J.L., P.W. and Y.W.; Investigation, J.L., P.W., H.Z., C.L., Z.L. and Y.W.; Resources, P.W., C.L. and Z.L.; Data curation, J.L.; Writing—original draft, J.L.; Writing—review & editing, J.L.; Visualization, J.L.; Supervision, P.W.; Project administration, P.W.; Funding acquisition, P.W. All authors have read and agreed to the published version of the manuscript.

Funding: This research received no external funding.

Data Availability Statement: No new data were created or analyzed in this study. Data sharing is not applicable to this article.

Conflicts of Interest: The authors declare no conflict of interest.

References

1. Cumming, I.G.; Wong, F.H. *Digital Processing of Synthetic Aperture Radar Data*; Artech House: Norwood, MA, USA, 2005; Volume 1, pp. 108–110.
2. Curlander, J.C.; Mcdonough, R.N. *Synthetic Aperture Radar: Systems and Signal Processing*; Wiley: Hoboken, NJ, USA, 1991.
3. Fan, W.; Zhou, F.; Zhang, Z.; Bai, X.; Tian, T. Deceptive jamming template synthesis for SAR based on generative adversarial nets. *Signal Process.* **2020**, *172*, 107528.1–107528.15. [CrossRef]
4. Zhao, B.; Huang, L.; Li, B.; Liu, S.-Q.; Bao, W.-M. One-bit splitting deceptive jamming against SAR. *Def. Technol.* **2022**, *18*, 1760–1777. [CrossRef]
5. Soumekh, M. SAR-ECCM using phase-perturbed LFM chirp signals and DRFM repeat jammer penalization. *Aerosp. Electron. Syst. IEEE Trans.* **2006**, *42*, 191–205. [CrossRef]
6. Chunrui, Y.; Xile, M.; Yongsheng, Z.; Zhen, D.; Diannong, L. Multichannel SAR ECCM based on Fast-time STAP and Pulse diversity. In Proceedings of the 2011 IEEE International Geoscience and Remote Sensing Symposium, Vancouver, BC, Canada, 24–29 July 2011.
7. Zhu, J.; Song, Y.; Jiang, N.; Xie, Z.; Fan, C.; Huang, X. Enhanced Doppler Resolution and Sidelobe Suppression Performance for Golay Complementary Waveforms. *Remote Sens.* **2023**, *15*, 2452. [CrossRef]
8. Chen, L.; Jindong, Z.; Qing, T.; Jia, H. Based on LFM-PC composite orthogonal modulation signal waveform design. *J. Signal Processing.* **2021**, *5*, 366–373.
9. Zhu, D. Sequence Set Design for a New LFM-PC Hybrid Modulated Radar Signal. *Sensors* **2021**, *21*, 5227.
10. Cheng, Y.; Zhang, J.; Li, C.; Zhu, D. Orthogonal anti-jamming waveform design with extended Doppler tolerance based on the LFM-PC signal. *Digit. Signal Process.* **2022**, *122*, 103334. [CrossRef]
11. Wang, Y.; Zhang, J.; Li, S.; Qiu, X.; Zhao, J. LFM-PC Hybrid Modulated Radar Signal Optimization Method Based on Alternating Direction Method of Multiplier. In Proceedings of the 2021 2nd China International SAR Symposium (CISS), Shanghai, China, 3–5 November 2021; pp. 1–8.
12. Sobhy, M.I.; Shehata, A.R. Chaotic radar systems In Proceedings of the 2000 IEEE MTT-S International Microwave Symposium Digest (Cat. No.00CH37017), Boston, MA, USA, 11–16 June 2000; Volume 3, pp. 1701–1704.
13. Wu, X.; Liu, W.; Zhao, L.; Fu, J.S. Chaotic phase code for radar pulse compression. In Proceedings of the 2001 IEEE Radar Conference (Cat. No.01CH37200), Atlanta, GA, USA, 3 May 2001; pp. 279–283.
14. Verdin, B.; Pappu, C.; Flores, B.C. Unified theory for wideband chaotic signal processing. In Proceedings of the 2014 IEEE Radar Conference, Cincinnati, OH, USA, 19–23 May 2014; pp. 729–734.
15. Walker; Tolle, W. *Chaotic Pseudorandom Sequences and Radar*; The University of Arizona: Tucson, AZ, USA, 1993.
16. Kai, D.; Ruliang, Y. Point target imaging simulation using chaotic signals. In Proceedings of the IEEE International Radar Conference, Arlington, VA, USA, 9–12 May 2005; pp. 847–850.
17. Hu, Y.; Zheng, Y.; Deng, Y. Research on anti-interference technology of hyperchaotic phase modulation signal. *J. Electron. Inf. Technol.* **2008**, *30*, 1756–1759. [CrossRef]
18. Qiu, X.; Wang, P.; Jiang, J.; Li, X.; Tang, Z.; Wang, S. Research on SAR Anti-jamming Technique Based on Orthogonal LFM-PC Signals with Adaptive Initial Phase. In Proceedings of the 2021 2nd China International SAR Symposium (CISS), Shanghai, China, 3–5 November 2021; pp. 1–5.
19. Hu, J.; Zhang, Y.; Li, Q.; Li, H.Y. Radar waveform design based on chaos synchronization and filtering. *Syst. Eng. Electron.* **2015**, *37*, 278–283.
20. Jiang, F.; Liu, Z.; Hu, W.; Bao, B. Waveform design of continuous chaotic frequency modulation radar with arbitrary Spectral structure. *Acta Electron. Sin.* **2010**, *38*, 2195–2198.

21. Pappu, C.S.; Carroll, T.L. Chaotic waveform for optimal joint radar communication systems. *Chaos Solitons Fractals* **2023**, *169*, 113261. [CrossRef]
22. Ying, S.; Shang, W.; Liu, G. Ambiguity function of chaotic phase modulated radar signals. In Proceedings of the Fourth International Conference on Signal Processing, Beijing, China, 12–16 October 1998.
23. Boukeffa, S.; Jiang, Y.; Jiang, T. Sidelobe reduction with nonlinear frequency modulated waveforms. In Proceedings of the 2011 IEEE 7th International Colloquium on Signal Processing and Its Applications, Penang, Malaysia, 4–6 March 2011; pp. 399–403.
24. Ashtari, A.; Thomas, G.; Kinsner, W.; Flores, B.C. Sufficient condition for chaotic maps to yield chaotic behavior after FM. *IEEE Trans. Aerosp. Electron. Syst.* **2008**, *44*, 1240–1248. [CrossRef]
25. Nobukawa, S.; Nishimura, H.; Yamanishi, T.; Doho, H. Induced Synchronization of Chaos-Chaos Intermittency in Coupled Cubic Maps by External Feedback Signals. In Proceedings of the 2018 5th International Conference on Control, Decision and Information Technologies (CoDIT), Thessaloniki, Greece, 10–13 April 2018; pp. 64–68.
26. Liu, H.-D.; Fan, J.-L.; Zhang, X.-F. A multi-piecewise Sine chaotic map and its performance analysis. In Proceedings of the 2022 14th International Conference on Measuring Technology and Mechatronics Automation (ICMTMA), Changsha, China, 15–16 January 2022; pp. 567–571.
27. Zhang, Q.; Xiang, Y.; Fan, Z.; Bi, C. Study of Universal Constants of Bifurcation in a Chaotic Sine Map. In Proceedings of the 2013 Sixth International Symposium on Computational Intelligence and Design, Hangzhou, China, 28–29 October 2013; pp. 177–180.
28. Goumidi, D.E.; Hachouf, F. Modified confusion-diffusion based satellite image cipher using chaotic standard, logistic and sine maps. In Proceedings of the 2010 2nd European Workshop on Visual Information Processing (EUVIP), Paris, France, 5–6 July 2010; pp. 204–209.
29. Bocheng, B.; Zhong, L.; Jianping, X. New chaotic system and its hyperchaos generation. *J. Syst. Eng. Electron.* **2009**, *20*, 1179–1187.
30. Tsubone, T.; Saito, T. Hyperchaos from a 4-D manifold piecewise-linear system. *IEEE Trans. Circuits Syst. I Fundam. Theory Appl.* **1998**, *45*, 889–894. [CrossRef]
31. Wolf, A.; Swift, J.B.; Swinney, H.L.; Vastano, J.A. Determining Lyapunov exponents from a time series. *Phys. D Nonlinear Phenom.* **1985**, *16*, 285–317. [CrossRef]
32. Wu, Y.; Fu, K.; Diao, W.; Yan, Z.; Wang, P.; Sun, X. Range Sidelobe Suppression Approach for SAR Images Using Chaotic FM Signals. *IEEE Trans. Geosci. Remote Sens.* **2022**, *60*, 5219915. [CrossRef]
33. Xie, S.; He, Z.; Hu, J.; Liu, L.; Pan, J. Performances of improved Tent chaos-based FM radar signal. *J. Syst. Eng. Electron.* **2012**, *23*, 385–391. [CrossRef]
34. Zhuang, L.; Dahl, J.; Zebker, H.; Jakovljevic, M. Applying the Chirp Scaling Algorithm for Efficient Beamforming of Ultrasound Images. In Proceedings of the IGARSS 2022—2022 IEEE International Geoscience and Remote Sensing Symposium, Kuala Lumpur, Malaysia, 17–22 July 2022; pp. 3011–3014.
35. Zhang, X.; Yang, P.; Sun, H. An omega-k algorithm for multireceiver synthetic aperture sonar. *Electron. Lett.* **2023**, *59*, e12859. [CrossRef]
36. Xie, Q.; Yang, J.; Liu, C.; Li, W. Low Sidelobe Quasi-Orthogonal NLFM Waveforms with Reciprocating Frequency Modulation. *IEEE Geosci. Remote Sens. Lett.* **2022**, *19*, 4027805. [CrossRef]